2019

Synchrotron Macro ATR-FTIR Microspectroscopy for High Resolution Chemical Mapping of Single Cells

Jitraporn Vongsvivut
Australian Synchrotron

David Perezguaita
Technological University Dublin, david.perezguaita@tudublin.ie

Bayden Wood
Monash University

See next page for additional authors

Recommended Citation

Vongsvivut, J. et al. (2019) Synchrotron Macro ATR-FTIR Microspectroscopy for High Resolution Chemical Mapping of Single Cells, *Analyst,* Issue 10, 2019. DOI:10.1039/C8AN01543K

Analyst

Accepted Manuscript

This article can be cited before page numbers have been issued, to do this please use: J. Vongsvivut, D. Perez-Guaita, B. R. Wood, P. Heraud, K. Khambatta, D. Hartnell, M. Hackett and M. Tobin, *Analyst*, 2019, DOI: 10.1039/C8AN01543K.

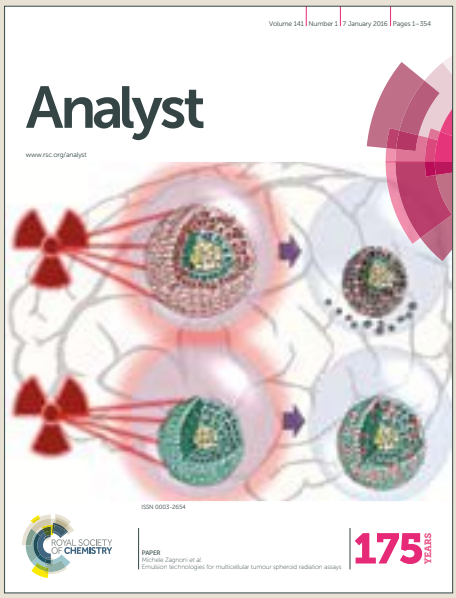

ROYAL SOCIETY OF CHEMISTRY

rsc.li/analyst

Synchrotron macro ATR-FTIR microspectroscopy for high-resolution chemical mapping of single cells

Jitraporn Vongsvivut,*[a] David Pérez-Guaita,[b] Bayden R. Wood,[b] Philip Heraud,[b,c] Karina Khambatta,[d,e] David Hartnell,[d,e] Mark J. Hackett[d,e] and Mark J. Tobin*[a]

[a] *Infrared Microspectroscopy (IRM) Beamline, Australian Synchrotron, 800 Blackburn Road, Clayton, Victoria 3168, Australia.*

[b] *Centre for Biospectroscopy, Monash University, Clayton, Victoria 3168, Australia.*

[c] *Department of Microbiology and Biomedicine Discovery Institute, Monash University, Clayton, Victoria 3168, Australia.*

[d] *Curtin Institute for Functional Molecules and Interfaces, School of Molecular and Life Sciences, Curtin University, GPO Box U1987, Perth, Western Australia 6845, Australia.*

[e] *Curtin Health Innovation Research Institute, Curtin University, GPO Box U1987, Perth, Western Australia 6845, Australia.*

** Corresponding authors:*

jitrapov@ansto.gov.au; tobinm@ansto.gov.au

Tel: +61 3 8540 4177 and +61 3 8540 4172; Fax: +61 3 8540 4200

View Article Online
DOI: 10.1039/C8AN01543K

Abstract

Attenuated total reflection Fourier transform infrared (ATR-FTIR) spectroscopy has been used widely for probing the molecular properties of materials. Coupling a synchrotron infrared (IR) beam to an ATR element using a high numerical aperture (NA) microscope objective enhances the spatial resolution, relative to transmission or transflectance microspectroscopy, by a factor proportional to the refractive index (*n*) of the ATR element. This work presents the development of the synchrotron macro ATR-FTIR microspectroscopy at Australian Synchrotron Infrared Microspectroscopy (IRM) Beamline, and demonstrates that high quality FTIR chemical maps of single cells and tissues can be achieved at an enhanced spatial resolution. The so-called "hybrid" macro ATR-FTIR device was developed by modifying the cantilever arm of a standard Bruker macro ATR-FTIR unit to accept germanium (Ge) ATR elements with different facet sizes (*i.e.* 1 mm, 250 μm and 100 μm in diameter) suitable for different types of sample surfaces. We demonstrated the capability of the technique for high-resolution single cell analysis of malaria-infected red blood cells, individual neurons in a brain tissue and cellular structures of a *Eucalyptus* leaf. The ability to measure a range of samples from soft membranes to hard cell wall structures demonstrates the potential of the technique for high-resolution chemical mapping across a broad range of applications in biology, medicine and environmental science.

View Article Online
DOI: 10.1039/C8AN01543K

1. Introduction

Spatially resolved molecular information is fundamental to analytical chemistry, making molecular characterisation techniques indispensable in a diverse range of research disciplines. Advances in optical technology over the past decades have resulted in state-of-the-art Fourier transform infrared (FTIR) microspectroscopic instrumentation developed by the integration of an IR transmission microscope into an FTIR spectrometer platform, providing a focused IR beam onto the sample and lateral resolutions from the millimetre to micron scales. As a result, FTIR microspectroscopy combines the versatility of a microscope through available spatial resolution, and the chemical sensitivity of the traditional FTIR spectroscopy, that enables microscopic examination of chemical distribution in complex heterogeneous materials such as biological cells and tissues. With the combination of multivariate data analysis approaches, FTIR microspectroscopy has further emerged as a powerful non-destructive and label-free analytical tool in the fields of biology and medicine.[1-4]

FTIR microspectroscopy using a conventional thermal source (Globar™) is compromised in applications where a highly focused beam is required. The low brightness (*i.e.* low photon flux density) results in a low signal-to-noise (S/N) ratio, and thereby poor spectral quality, when confining the IR beam into a small spot using small apertures.[5, 6] To overcome this limitation and achieve high S/N ratio at a spatial resolution sufficient for a single cell measurement, a broad-band high-brightness synchrotron IR beam from a storage ring can be coupled to a FTIR microspectroscopic system located at the end station of the beamline.[5, 6] The highly collimated synchrotron IR beam essentially offers 100−1000 times higher brightness than a broad-band Globar™ IR source commonly used in a laboratory-based FTIR microspectroscopic instrument.[5, 7, 8] The superior characteristics of high photon flux density and diffraction-limited spatial resolution with enhanced spectral quality in terms of S/N ratio achieved by synchrotron FTIR microspectroscopy, are the key requirement that allows for

View Article Online
DOI: 10.1039/C8AN01543K

spatially resolved chemical mapping measurement of heterogeneous materials. In addition, the mid-IR photons generated from a synchrotron source are too low in energy to directly break molecular bonds in the exposed sample, and the heating effect of the synchrotron IR source has been shown to be negligible making it a non-destructive approach.[9] The technique enables molecular characterisation of individual cells or a single microorganism;[6, 10-12] however most sub-cellular detail excepting the nucleus cannot be resolved.

Attenuated total reflection (ATR) FTIR spectroscopy utilizes the property of total internal reflection established when light traveling in an optically denser medium of an ATR crystal element impinges onto the surface of a lower-index medium with an incident angle greater than the critical angle.[13] Under these specific conditions, the electromagnetic field (*i.e.* an evanescent wave) penetrates and decays exponentially within a shallow depth of the adjacent lower-index sample. Any IR-absorbing material located in contact with this interface interacts with the evanescent field resulting in an IR absorption, which is consequently transformed into an ATR-FTIR spectrum. The typical path lengths that the evanescent wave penetrates into most organic samples, are generally described in terms of depth of penetration (d_p), which is defined as the distance where the strength of the electric field decays to e^{-1}.[13, 14] The depth of penetration ranges from 0.2 μm to 5 μm, depending on the refractive indices of the ATR crystal (n_0) and the sample (n_1), the angle of incidence (θ) and the wavelength of light (λ), as given by Eq. 1.[13, 14] Hence, the ATR-FTIR technique has been widely used for probing molecular information of materials. In particular, the technique has been used as an effective sampling method (*i*) when the sample cannot be prepared as thin sections for transmission measurements, and (*ii*) to avoid scattering artefacts commonly encountered in transflectance measurements.

$$d_p = \frac{\lambda}{2\pi n_0 \sqrt{\sin^2\theta - \left(\frac{n_1}{n_0}\right)^2}} \quad (1)$$

Microscopic ATR-FTIR (micro ATR-FTIR) is the conventional method for performing an ATR-FTIR measurement in a microscopic configuration. With micro ATR-FTIR, the ATR crystal is attached to the front of the microscope objective and a mapping measurement is performed with repeated contacts between the sample and the ATR sensing surface similar to a tapping mode. Such an approach has several disadvantages. First, the high contact pressure repeatedly applied on each measurement point may cause damage to the surface of the sample and can lead to cross contamination of the subsequent measurement positions, limiting the applications of the technique to only those with durable surfaces. Second, the release-and-contact process results in a slow mapping measurement. An alternative approach for performing ATR-FTIR microspectroscopic measurements was first reported by Lewis and Sommer, based on the use of a large ATR hemispherical element and a single-point detector in mapping mode.[15, 16] The technique has been progressively developed using imaging detectors and were reported as microspectroscopic imaging,[17-19] macro ATR-FTIR imaging,[20, 21] micro and macro ATR-FTIR spectroscopic imaging techniques.[22-24] The technique increases the field of view and only requires a single contact point for the entire mapping measurement. Using an ATR optical element of high refractive index essentially leads to the reduction of both the diffraction-limited beam size at the microscope's focus and the mapping step size (relative to the stage step motion) by the factor of the refractive index (n) of the ATR material, thereby improving spatial resolution.[15-17, 22] As a result, the macro ATR-FTIR approach overcomes the limitations experienced with the micro ATR-FTIR approach and opens up a new opportunity for high-resolution chemical analysis of biological and other materials.

This work presents advances in the synchrotron macro ATR-FTIR microspectroscopic technique based on one of the two models developed for mapping measurements at Australian Synchrotron IR Microspectroscopy (IRM) Beamline. While one of our macro ATR-FTIR models was developed based on a piezo-controlled translation system,[25] the so-called "hybrid"

macro ATR-FTIR device used in this study, is an adaptation of a standard macro ATR-FTIR unit (Bruker Optik GmbH, Ettlingen, Germany). The advantages and disadvantages of the technique, compared to other FTIR mapping and imaging approaches (*e.g.* micro ATR-FTIR, transflectance and transmission), are discussed in detail. The capability of the technique for high-resolution single cell analysis are demonstrated using malaria-infected red blood cells (RBCs), individual neurons in brain tissue and the surface chemistry of a *Eucalyptus* leaf, as models to represent applications in biology, medicine and environmental science, yet the technique is suited to all forms of soft and hard materials.

2. Materials and methods

2.1 Malaria-infected RBCs

Materials and Reagents. Whole blood, provided under a Material Supply Agreement with the Australian Red Cross Blood Service (Material Supply Deed 17-11VIC-06), was centrifuged at 1500 rpm for 5 min to remove the plasma. The RBCs were then used for *in-vitro* culture of *Plasmodium falciparum* parasites (laboratory strain D10). All chemicals used in this study were of analytical grade and purchased from Sigma-Aldrich (Australia) and Merck Chemicals (Australia).

Biological Methodology. The *in-vitro* culture of *Plasmodium falciparum* parasites (laboratory strain D10) at 3% haematocrit was performed using RPMI media supplemented with 10% AlbuMAX II (Gibco, Thermo Fisher Scientific, Victoria, Australia). The infected RBCs were centrifuged to remove culture media and cleaned with a 1% NaCl solution following synchronising of trophozoite-stage parasites to 5% parasitemia. Thin smears of the infected RBCs were deposited on CaF_2 slides, air-dried, fixed in methanol for 5 min and then allowed to air dry again. Detailed information on the sample treatment was previously published elsewhere.[26]

View Article Online
DOI: 10.1039/C8AN01543K

2.2 Brain tissue

Animal Models. Brain tissue was harvested from a single 12-month-old wild-type mouse (C57BL/6), which was surplus to needs from a larger time course study comparing normal and accelerated ageing. Mice were housed in standard cages in a temperature controlled (21 °C) colony room on a 12 h/12 h light/dark cycle with standard rodent maintenance chow and water available *ad libitum*. All animal procedures were performed in accordance with the Australian Code for Care and Use of Laboratory Animals at Curtin University and approved by the Animal Research Ethics Committee of Curtin University.

Tissue Collection and Sample Preparation. To avoid sample preparation-introduced chemical artefacts, mice were anaesthetised with pentobarbitone (45 mg/kg) and humanely sacrificed. The brain tissue was rapidly removed from the skull and immediately flash frozen in liquid nitrogen-cooled isopentane, as described previously.[27-29] The indicated method preserves the chemical makeup of the brain tissue very close to the *in vivo* condition. Five-micron-thick coronal brain sections (−2 mm anterior to Bregma) were cut with a cryo-microtome at −18 °C and melted onto regular glass microscope slides for synchrotron ATR-FTIR measurements. Additional tissue sections were prepared on CaF_2 windows and Si_3N_4 substrates for transmission mapping (CaF_2) and multi-modal wide-field FTIR imaging with a focal plane array (FPA) detector (CaF_2), and x-ray fluorescence elemental mapping (Si_3N_4) experiments.

2.3 *Eucalyptus* leaf

Materials. The *Eucalyptus* leaf used in this study is part of a larger investigation of seasonal variation in epicuticular wax composition on the surface of leaves of different *Eucalyptus* species. This study reports a representative example of the data that can be obtained using the synchrotron macro ATR-FTIR analysis of *Eucalyptus* leaves. The specific example

is a leaf collected from a yellow gum tree, identified to be *Eucalyptus leucoxylon*. The leaves were trimmed with a scalpel to approximately 3 × 3 cm^2 and analysed directly without any further sample preparation. The leaf was harvested from the tree at the end of daylight (sunset) and the analysis was commenced within 2 h of harvest.

2.4 Synchrotron ATR-FTIR mapping microspectroscopic methodology

Synchrotron FTIR measurements were performed at the Australian Synchrotron IRM Beamline (Victoria, Australia), using a Bruker Vertex 80v spectrometer coupled with a Hyperion 2000 FTIR microscope and a liquid nitrogen-cooled narrow-band mercury cadmium telluride (MCT) detector (Bruker Optik GmbH, Ettlingen, Germany). Details of the layout and end stations/branch lines of the beamline were published elsewhere.[30] All synchrotron FTIR spectra were recorded within a spectral range of 3800–700 cm^{-1} using 4 cm^{-1} spectral resolution. Blackman-Harris 3-Term apodisation, Mertz phase correction, and zero-filling factor of 2 were set as default acquisition parameters using OPUS 7.2 software suite (Bruker Optik GmbH, Ettlingen, Germany).

Synchrotron macro ATR-FTIR mapping measurements were performed using the in-house adapted macro ATR-FTIR device equipped with a Ge ATR hemispherical crystal (n_{Ge} = 4) having a 250 μm diameter sensing facet, and using a 20× IR objective (NA = 0.60; Bruker Optik GmbH, Ettlingen, Germany).[31-33] The malaria-infected RBCs were dried and fixed onto a 0.5 mm thick CaF_2 window, whilst brain tissue and *Eucalyptus* leaf were mounted on separate glass slides. The microscope glass slides were then directly placed on an aluminium disc using double-sided polyimide (Kapton®) tape. After that, the aluminium disc was placed into the sample stage of the macro ATR-FTIR unit. The Ge ATR crystal was then brought into the focus of the synchrotron IR beam below the 20× IR objective and, when the humidity in the nitrogen-purged enclosure surrounding the microscope stage had dropped to ~20%, a

background spectrum was recorded in air using 256 co-added scans. The sample was then brought into contact with the Ge ATR crystal, and a rapid low resolution overview synchrotron macro ATR-FTIR chemical map was initially acquired to determine the area and the quality of the sample contact, at a 20 μm step interval, using 8 co-added scans. A subsequent synchrotron macro ATR-FTIR mapping measurement was performed on specific locations within the overview map where a good contact with the Ge ATR crystal was identified, using a smaller step interval of 0.25 μm and 16 co-added scans for RBCs, 0.25 μm step interval and 4 co-added scans for brain tissue, and 0.50 μm step interval and 8 co-added scans for the *Eucalyptus* leaf.

To evaluate the spatial resolution improvement in an applied scenario, studying neurons *in situ* within thin sections of brain tissue using synchrotron FTIR mapping in transmission geometry (transmission-FTIR mapping) and multi-beam wide-field FTIR imaging analyses were also carried out. Detailed methods for the analysis of brain neurons in brain tissue at the Australian Synchrotron have previously been reported for transmission-FTIR mapping,[27, 34] and FPA-FTIR imaging.[30]

Specifically, synchrotron transmission-FTIR maps were collected with a matching 36× objective and condenser (NA = 0.50; Bruker Optik GmbH, Ettlingen, Germany), a projected aperture size of 4.2 μm, and a 1 μm mapping step size (effective pixel size of 1 μm). Spectra were collected at 4 cm^{-1} spectral resolution, with the co-addition of 4 scans, and a background spectrum collected from a blank CaF_2 substrate with the co-addition of 256 scans. Spectral resolution was converted to 8 cm^{-1} post data collection, to simplify comparison with synchrotron FPA-FTIR imaging and synchrotron macro ATR-FTIR mapping data.

Synchrotron FPA-FTIR imaging data were collected with a 52× objective (NA = 0.65; Edmund Optics, Singapore) and a 20× condenser (NA = 0.60; Bruker Optik GmbH, Ettlingen, Germany), which yielded an effective pixel size of 0.77 μm.[30] Spectra were collected at 8

cm^{-1} spectral resolution, with the co-addition of 128 scans, and a background spectrum collected from a blank Si_3N_4 substrate with the co-addition of 128 scans.

2.5 Spectral pre-processing and multivariate data analysis approaches

Malaria-infected RBCs. Data was treated using Matlab from Matworks (Natick, MA, USA). In-house written functions, as well as functions from PLS-Toolbox (Eigenvector Research Inc., Manson, WA, USA), were employed for importing, pre-processing and clustering the hyperspectral images. K-Means clustering analysis (KMCA) was performed using the function *kmean* from the statistical toolbox in Matlab. The computation was parallelised and different numbers of classes (3−7) were used as inputs. The Savitzky-Golay algorithm was employed for computing the second derivative of the spectra (15 points window and 2 degree polynomial).[35] Data was also normalised using the standard normal variate approach (SVN) and mean centred.

Brain tissue and *Eucalyptus* Leaf. FTIR spectra from each spectral image were first extracted and quality-screened using CytoSpec™ v. 1.4.02 (Cytospec Inc., Boston, MA, USA). False colour chemical images were then generated based on integrated areas under specific absorption peaks, to show the distribution and abundance of these functional groups. In particular, methylene groups $\nu_s(CH_2)$ in the spectral range of 2840–2865 cm^{-1}, was used as a spectroscopic marker of lipid distribution (brain tissue) and epicuticular wax distribution (*Eucalyptus* leaf). On the other hand, methyl groups $\nu_s(CH_3)$ in the spectral range of 2870–2885 cm^{-1}, was used as a spectroscopic marker to localise the cell wall, which has a relative abundance of molecular species enriched in methyl groups (*Eucalyptus* leaf), and a methyl : methylene ratio to reveal the location of the nucleus inside brain neurons, as used previously.[28]

View Article Online
DOI: 10.1039/C8AN01543K

3. Results and discussion

3.1 Synchrotron macro ATR-FTIR mapping microspectroscopic technique (technical perspectives)

As illustrated in Fig. 1A, the hybrid macro ATR-FTIR device incorporated a standard Bruker macro ATR-FTIR base unit, which was further adapted by replacing the standard cantilever arm with an in-house designed cantilever to accept Ge micro-ATR elements. While the standard macro ATR-FTIR unit was originally equipped with a large 1-mm-diameter facet Ge hemisphere crystal (Fig. 1A, label ❶), the hybrid macro ATR-FTIR device was designed to fit Ge micro-ATR crystals of two different facet sizes including 250 μm and 100 μm diameters (Fig. 1A, label ❷). Because the quality of the contact between the sensing surface of the ATR crystal and the sample plays a crucial role in achieving a high S/N ATR-FTIR spectra, having different facet sizes available offered a range of contact pressures to suit the different types of sample surface. The large Ge macro-ATR facet size is most suited to soft and delicate materials that require no or only minimal pressure in order to achieve good contact such as thick tissue and fingermarks.[36] The smaller diameter micro-ATR tips, on the other hand, can provide medium to high pressure levels. In particular, the 250 μm diameter Ge tip has been found to suit a wide range of samples.[32, 33, 37] The 100 μm diameter tip provides a higher pressure at the sample surface, and allows measurement of small and narrow regions with limited access, making it suitable for hard and rough surfaces. For temperature-controlled and temperature-dependent studies, a modified sample stage has been developed (Fig. 1B) incorporating temperature-controlled water circulation and a temperature probe.

Coupling the synchrotron IR beam through the Ge ATR hemispherical crystal ($n_{Ge} = 4$) using a microscope objective effectively reduces the beam focus size by a factor of 4, as a result

View Article Online
DOI: 10.1039/C8AN01543K

of the numerical aperture (NA) of the focused beam, and hence the Rayleigh diffraction limit, being dependent upon on the refractive index of the Ge through which it is focused, as given by Eq. 2.

$$r = \frac{1.22\lambda}{2NA} = \frac{1.22\lambda}{2n\sin(\theta)} \quad (2)$$

where r is the separation distance at which two objects are just resolved, λ is the wavelength of light, n is the refractive index of the Ge ATR crystal (in this case), and θ is the half-angle of the focusing cone of the light entering the Ge ATR crystal from the microscope objective.

It should be noted that the separation required to resolve the two adjacent points completely in mid-IR spectroscopy with the wavelength range of 5–20 μm, is reportedly 2r due to various optical aberrations.[17, 22, 38] Furthermore, based on the fact that only half of the objective aperture is being employed to introduce the beam into the ATR crystal in a reflectance optical configuration, the numerical aperture of the objective should be reduced by a factor of 2,[17] which results in NA = 0.30 in this case. Under this condition, the optimal calculated spatial resolution (2r) of a macro ATR-FTIR setup using a Ge hemispherical crystal (n_{Ge} = 4) is 3.48 μm at a wavelength of 3.42 μm equivalent to ν_{as}(C–H) mode of methylene groups at 2925 cm^{-1}, which we used in this study to determine the experimental spatial resolution value. Therefore, the calculation suggests that the optimal spatial resolution of these macro ATR-FTIR measurements is likely to be approximately the wavelength of the mid-IR light, whilst the optimal spatial resolution (2r) expected for transmission and transflectance modes (in air) at 2925 cm^{-1}, is 6.95 μm and 13.90 μm, which is two and four times poorer that than that calculated based on the macro ATR-FTIR condition, respectively.

To determine the spatial resolution achievable with our optical configuration, the synchrotron macro ATR-FTIR mapping measurement of a photoresist polymer bar was

performed using a Ge hemispherical crystal with 250 μm diameter sensing facet at 0.25 μm step interval across the entire width of the polymer bar. The synchrotron macro ATR-FTIR spectrum of the 2 μm thick photoresist polymer used in this study is illustrated in the ESI (Fig. S1). Figure 2 shows the macro ATR-FTIR absorbance maps of the photoresist polymer bar, produced based on normalised absorbance at 2925 cm^{-1} for ν_{as}(C–H) stretching mode, which were acquired at the three smallest projected apertures available at the beamline. Following the line scan approach,[17, 18, 22, 38] the normalised absorbance values were plotted as a function of the distance across the polymer width, and two values of spatial resolution corresponding to 5% and 95% of the maximum absorbance were obtained on both sides of the polymer bar in each map. The average spatial resolution was found to be 3.50 μm, 3.15 μm and 2.95 μm at three decreasing projected apertures of 3.13 μm, 2.50 μm and 1.88 μm, respectively. The reason that the spatial resolution was only slightly improved with decreasing projected apertures is due to the intrinsically small source size of the synchrotron beam. The focused spot of the synchrotron IR beam without an applied aperture is close to the diffraction limited for the optical system employed for this study. This measurement demonstrates that the achievable spatial resolution for this specific synchrotron macro ATR-FTIR configuration was ~3.20 μm, which is very close to the calculated value (*i.e.* 3.48 μm).

To further evaluate the experimental spatial resolution in the fingerprint region where the majority of the biological bands are present, the normalised absorbance at 1607 cm^{-1} characteristic of ν(C–C) aromatic ring stretching mode of the photoresist polymer was selected for the calculation using the same 5%–95% line scan approach applied previously. The measured spatial resolution in the fingerprint region, which is presented the ESI (Fig. S2), was 4.35 μm, 4.20 μm and 3.88 μm at the projected apertures of 3.13 μm, 2.50 μm and 1.88 μm, respectively. Similar to the previous observation at the high wavenumber region, the spatial

resolution in the fingerprint region was only slightly improved with decreasing projected apertures due to the small intrinsic source size of the synchrotron IR beam. As expected, the spatial resolution was found to be poorer than that measured using the absorbance in the high wavenumber region due to the dependence of spatial resolution on the wavelength of light and the numerical aperture of optical system.[8] It is notable that the spatial resolution at 1607 cm^{-1} was not degraded proportional to wavenumber, when compared with the resolution at 2925 cm^{-1}. This may be due to the contribution from the edge profile of the polymer test target to the observed absorbance profile, and the wavelength dependence of the emission angle of synchrotron radiation from the electron storage ring. This latter effect could contribute to lower efficiency of illumination of the objective entrance pupil at shorter wavelengths.[39] Nevertheless, it is important to emphasise that the spatial resolution reported in this study was evaluated using an interface between a very thin photoresist polymer and an IR-transmitting substrate (CaF_2). As a result, these values may differ from the actual spatial resolution obtained in the measurements of biological samples, where all domains will be absorbing in the spectral regions of interest.

In essence, the magnification factor associated with the refractive index (n) of the ATR crystal not only leads to a four times improvement in the spatial resolution, but also allows the measurement to be performed with aperture sizes that are n times larger, thereby eliminating the diffraction effects introduced by small aperture dimensions. Since the sample in macro ATR-FTIR mode remains in contact with the ATR crystal throughout the mapping measurement, unlike the point-to-point micro ATR-FTIR mapping technique, the mapping step size is also decreased by the same proportion (*i.e.* by a factor of 4) relative to the physical step motion of the sample stage. 2D mapping measurements can be performed on a motorised sample stage at the minimum physical step motion of 1 μm, which effectively produces 0.25 μm translation step through the Ge crystal in the macro ATR-FTIR mode. Based on the optical

setup of the microscope at the beamline, the half-angle of the focusing cone is estimated to be 36.9°.[32] Taking this as the angle of incidence, and using Eq. 1, the depth of penetration of the evanescent wave in contact with a biological sample ($n_1 \cong 1.35$) is approximately 0.5 μm at 1650 cm^{-1} for the Amide I band. The outstanding advantages of the enhanced spatial resolution, when compared to transmission or transflectance approaches, therefore enable the synchrotron macro ATR-FTIR microspectroscopic mapping technique to be used for high resolution chemical characterisation.

The other advantage of the ATR-FTIR microspectroscopy based on a single-bounce geometry is the enhancement of collection efficiency of light, resulting in an increase of the overall energy throughput of the measurement. Figure 3A illustrates changes in throughput intensity of the synchrotron IR beam mapped across the flat sensing surface of the three Ge ATR crystals (*i.e.* 1 mm, 250 μm and 100 μm in diameter). These 2D images of the throughput intensity were found to be best displayed in grayscale to achieve optimal contrast, and to represent the linear relation between the grey colour level and the intensity. As expected, the throughput in all cases was most intense within the middle region of the Ge sensing facets where the centre of the Ge hemisphere crystal aligned with the optical axis of the microscope, and then dropped rapidly with increasing distance away from the central optical axis. In addition, the throughput maps revealed that the synchrotron IR signals dropped more rapidly along the horizontal *x*-axis than the vertical *y*-axis. According to the intensity profiles, the active areas where throughput signals are above the baseline were approximately 20%, 40% and 95% of the total facet surface for 1 mm, 250 μm and 100 μm crystals, respectively. Only the 100 μm diameter tip offered full-size mapping area relative to its facet surface, while the other two crystals were under-filled particularly with the standard 1 mm diameter crystal that showed a larger area of weak signals. This observation suggested that, in terms of effectiveness for the mapping area, the hybrid macro ATR-FTIR device equipped with micro-ATR crystals

is more effective for coupling the synchrotron IR beam into the crystal, than the standard unit. Nevertheless, the limited mapping area available for each tip size represents a trade-off for obtaining high lateral resolution.

Figure 3B presents the plot of maximum throughputs measured at the centre of the optical axis at different projected aperture sizes. The result obtained from all three crystals showed a similar trend with only slightly lower overall throughput observed for the smallest 100 μm diameter tip. The throughput signal observed with the full synchrotron IR beam at the projected aperture size of ~9 μm in diameter started to gradually decrease when further reducing the projected aperture size down to ~1.88 μm. Based on their corresponding single beam spectra in Fig. S3, the cut-off for the three smallest apertures was found at ~1000 cm^{-1}. By opening up the aperture to obtain a larger beam size, the long wavelength cut-off was shifted towards 900 cm^{-1}, allowing an investigation of bands in the spectral range of 900−1000 cm^{-1}.

3.2 Malaria-infected RBCs

Figure 4 summarises the results of the data treatment from a hyperspectral image of a RBC infected with a *Plasmodium falciparum* trophozoite, measured with a step size of 2 μm. Figure 4A shows a visible image from a smear of RBCs. The cell indicated with the yellow outline contains a circular shape in the middle, suggesting the presence of a trophozoite in the active growing stage of the malaria parasite. The false colour map available in Fig. 4B represents the absorbance at 1650 cm^{-1} (blue to red indicates low to high absorbance). This wavenumber was selected because it is assigned to the Amide I band, associated with the proteins, as shown in the reference spectra presented in Fig. 4F. RBCs are mainly composed of haemoglobin, which correlates well with the concentration of protein in RBCs shown in the visible image (see the overlay in Fig. 4D). The overlay also indicates low protein content inside the parasite. This can be due to a lower proportion of proteins in the trophozoite, compared with uninfected normal

RBCs, or to a scattering effect produced by the parasite.[40, 41] Figure 4C shows a false colour image based on the integrated area of the second derivative band minimum at 1710 cm^{-1} (blue to red indicates low to high values). This band is related to the presence of haemozoin (Hz), a by-product of the haemoglobin catabolism produced by the *Plasmodium* parasite. Figure 4E shows correlation between the magnitude of the integrated area of the second derivative band minimum and the location of the parasite.

Results indicated that the synchrotron macro ATR-FTIR configuration was able to identify a single RBC infected with the *Plasmodium* parasite. A further image of the infected RBC was collected at higher resolution, using a 0.50 μm pixel size (Fig. 5). Figure 5A presents a 3D image of the intensity of the Amide I (1640 cm^{-1}), showing a close-up of the decrease of the intensity in the middle of the cell mentioned above. Figure 5B shows the K-means clustering analysis performed over the hyperspectral image, which classified the pixels in 4 different classes. Whilst the blue, orange and yellow classes did not show any spatial clustering, pixels from the violet class were concentrated in the centre of the cell, *i.e.* where the parasite was located. The second derivative of the average spectrum of each class is shown in Fig. 5 (C-E), and gives information about the chemical composition. Red, blue and yellow classes show similar spectral profiles, confirming the homogeneous composition of these classes, which appeared scattered around the image. The average spectrum of the violet class shows distinctive spectral features. In particular, the negative peak around 1713 cm^{-1} (Fig. 5C) can be assigned to the stretching vibrations of the carboxylate groups of Hz,[42] as illustrated in Fig. 4F. The two bands found in the C–H stretching region at 2908 cm^{-1} and 2850 cm^{-1} (Fig. 5D) were also found in the reference spectrum of Hz. Finally, the second derivative of the Amide I band in the spectral range of 1670-1630 cm^{-1} (Fig. 5E) shows a shift in the maximum of the band towards 1660 cm^{-1}. This may indicate the presence of the Hz carboxylate at 1661 cm^{-1} band. In

summary, there is strong evidence that the spectral features found in the violet spectral class correspond to the presence of Hz in the centre of the RBC.

It can be concluded that the synchrotron macro ATR-FTIR mapping microspectroscopy was able to localise and chemically characterise the parasite inside the RBC. To put this in context, the significance of the results should be compared with other available IR imaging techniques. FTIR spectroscopy has been extensively used for the study of *Plasmodium* parasites, being a powerful tool for characterising changes in the chemistry of the RBC-parasite system.[43] For example, the technique has been used as a diagnostic tool[44] and for the evaluation of the effect of antimalarial drugs.[45] The main drawback of the technique has been the spatial resolution. The limitation in spatial resolutions of mid-IR light (2.5−25 μm) makes its application challenging in the study of small cells such as RBCs (8 μm) and parasites (1−3 μm). Therefore, spectral analysis is normally performed on average spectra from a bulk measurement in conventional ATR-FTIR or as an average spectrum of a single cell. This, however, implies that the resulting spectrum represents the composition of both the parasite and RBC, and the signal of the high concentrated haemoglobin present in the uninfected part of the RBC can mask spectral signatures of the parasite. Further efforts have been focused on imaging infected RBCs with sub-cellular resolution to acquire spectra from just the parasite. This would allow one to retrieve high quality information about the chemical composition of the parasite without interference of the host cell. Regions within RBCs where IR spectral signatures of the *Plasmodium* parasite have previously been identified using supervised models over the C−H stretching region,[46] or through a multi-modal approach that combines Raman spectroscopy and FTIR imaging to flag specific parasite pixels.[26] In both cases, haemozoin and lipid signals were weak and, although they were indicative of the presence of the parasite, they were not intense enough to be used as markers for changes in the parasite phenotype.

To date, the low resolution of the conventional FTIR technique has been the major limiting factor for determining the chemical characterisation of the parasite, which has only recently been achieved using the combination of atomic force microscopy (AFM) and IR.[47] In contrast, results presented in Figs. 4 and 5 illustrate that synchrotron macro ATR-FTIR mapping microspectroscopy can confirm the presence of *Plasmodium falciparum* parasites in single RBCs without the need of an AFM-IR instrument. In summary, synchrotron macro ATR-FTIR mapping microspectroscopy clearly outperformed synchrotron FTIR microspectroscopy in transmission setup in terms of spatial resolution and sensitivity. However, the technique does require close contact with the fragile RBC sample and care must be taken to avoid damaging the cell.

3.3 Neurons in brain tissue

Transmission FTIR mapping and imaging modalities have previously been shown capable of resolving individual brain cells, such as neurons, and resolving larger sub-cellular organelles such as the nucleus within the neuron.[48-50] Neurons themselves have relatively low lipid content compared to surrounding brain tissue (referred to as the neuropil), and within the neuron, the cytoplasm has higher lipid content than the nucleus, which is almost devoid of lipids. Although low in lipid content, the abundance of acetylated proteins within the nucleus gives rise to a relatively high content of methyl groups. These molecular characteristics have been previously used as spectroscopic markers to identify neurons and to differentiate between the nucleus and cytoplasm,[48, 49] for example false colour function group images generated from the integrated area under the curve of the $\nu_s(CH_2)$ absorbance band reveal the neuropil (high absorbance), and this allows identification of the neuron body based on low absorbance. Within the neuron body, the nucleus can be identified by an increased ratio of $\nu_s(CH_3)$ to $\nu_s(CH_2)$ absorbance. False colour images of these spectroscopic markers are presented for a representative example of a

brain neuron mapped with the synchrotron macro ATR-FTIR microspectroscopic technique. As expected, poor image contrast exists in unstained brain tissue, making identification of the neuron body difficult (Fig. 6A, E); however, the false-colour FTIR functional group images generated from methylene groups (Fig. 6B), the methyl to methylene ratio (Fig. 6C) and the two-colour overlay (Fig. 6D), provide the ability to resolve the neuron location, and identify the nucleus. Furthermore, the lipid rich neuropil appears to be bisected by a series of low lipid regions that branch from the main neuron body (Fig. 6B, D and white-dashed outline in Fig. 6F). Each of the branches is approximately 1–2 μm thick, which is consistent with neuron-dendrite morphology. Neuron dendrites have not previously been resolved with synchrotron transmission FTIR measurements (including both single point mapping, and multi-beam FPA imaging), yet it appears that the improved spatial resolution of the synchrotron macro ATR-FTIR mapping approach may enable these structures to be resolved. Dendrites hold critical roles in neuron signalling, and the ability of the macro ATR-FTIR mapping technique to directly study the chemical composition of neurons, without the use of labels or stains, may find a wide range of applications in the neurosciences. At this stage, however, our results must be interpreted with caution, as removal of the brain tissue from the Ge crystal tip disrupts that portion of the sample, making staining and histological confirmation of the dendrite location post ATR-FTIR analysis impossible.

To demonstrate the improved spatial resolution of the synchrotron macro ATR-FTIR mapping measurements, a comparison of three synchrotron FTIR microspectroscopic modes including macro ATR-FTIR mapping, multi-beam FPA-FTIR imaging and transmission-FTIR mapping, for representative brain neurons is presented in Fig. 7. The images visually highlight greater spatial detail and improved ability to discern neuron morphology in the synchrotron macro ATR-FTIR data compared to the transmission-FTIR mapping and FPA-FTIR imaging. The improved spatial resolution is further demonstrated by a reduction in the effect of spectral

blending in the synchrotron ATR-FTIR data. As discussed above, the nucleus is largely devoid of lipids, and therefore contains a very low $\nu_s(CH_2)$ signal. In each of the examples presented in Fig. 7, the pixel size is less than the size of the nucleus; however, the theoretical diffraction-limited spatial resolution is much greater than the pixel size in the case of transmission-FTIR mapping and FPA-FTIR imaging. Thus, spectral blending is expected to occur in these cases, and although the nucleus can be resolved with transmission-FTIR mapping and FPA-FTIR imaging, a stronger $\nu_s(CH_2)$ signal is observed in spectra extracted from the nucleus, which is likely due to spectral blending from the cytoplasm. Although Figures 6 and 7 highlight the spatial resolution advantage of the macro ATR-FTIR mapping technique, Figure 7 demonstrates that measurement time is substantially longer, due to the requirement to collect a greater number of pixels at smaller step sizes. Future developments coupling linear array or FPA imaging detector with the macro ATR-FTIR modalities may therefore offer an attractive imaging pathway for rapid sub-cellular biochemical imaging.

3.4 Surface chemistry of *Eucalyptus* leaf

Thus far, this manuscript has described applications of the synchrotron macro ATR-FTIR mapping microspectroscopy to mammalian cells and applications in the health sciences. However, the ability to study biochemical distribution at sub-micron, sub-cellular spatial resolution is of wider value in the biological sciences. To demonstrate this potential, we report a specific example of studying epicuticular wax distribution on the surface of *Eucalyptus* leaves. Epicuticular waxes on the leaf surface are critical to plant health and physiology.[51, 52] The wax content is regulated by plant lipid metabolism, which can reflect levels of plant stress induced by the surrounding environment, nutritional content of soil or climate change.[52, 53] Therefore, epicuticular waxes can be an important external chemical marker of internal plant health, and provide insights into plant response to climate change, rising soil acidity or salinity,

poor soil nutrition, and other factors.[52, 53] Bulk analysis of plant leaf epicuticular waxes is routinely performed, and an important analytical measurement in the plant sciences.[51, 52, 54] However, the ability to directly image the distribution of, and obtain chemical information about, epicuticular waxes, is novel to the field. Electron microscopy (EM) is capable of indirect measurement of wax distribution, and although capable of providing nanoscale spatial resolution of surface wax morphology, it does not directly differentiate between different wax components.[54, 55]

Synchrotron macro ATR-FTIR mapping microspectroscopy has the potential to fill the gap between bulk analysis of epicuticular wax composition and EM imaging at nanoscale spatial resolution. Figure 8 shows an example of the synchrotron macro ATR-FTIR mapping result revealing the distribution, at a resolution of a few microns, of multiple chemical constituents on the surface of a *Eucalyptus* leaf (*Eucalyptus leucoxylon*). The composite image displayed in Fig. 8E shows that a heterogeneous wax distribution based on the intensity of the methylene groups is observed, with the greatest wax content found between cell walls (rich in methyl groups). This capability to study epicuticular wax distribution at high spatial resolution, and the ability to correlate wax constituent with plant anatomical structures, such as the cell wall and stomata cells, may be of great benefit to future experimental studies investigating effects of plant stress on plant lipid metabolism and epicuticular wax formation.

4. Conclusion

In this report, several case studies were presented that demonstrate the versatility of synchrotron macro ATR-FTIR mapping microspectroscopy developed at the Australian Synchrotron for high-resolution chemical mapping measurement of single cells. The selection of the appropriate sample substrate and ATR crystal depends on the system being studied, and also on the required spatial resolution, field of view, sample type, and desired experimental

conditions. Because ATR-FTIR spectroscopy is based upon the evanescent field, the technique allows the analysis of thick sections as well as other strongly absorbing materials, with only minimal sample preparation required and , whilst avoiding the spectral artefacts often introduced by scattering. The reported synchrotron macro ATR-FTIR mapping microspectroscopy can be applied to analyse a diverse range of samples and systems with high resolution and chemical specificity, and will have many applications in active areas of spectroscopic research such as biology, medicine and environmental science.

Acknowledgements

This research was undertaken on the IRM beamline at Australian Synchrotron (Victoria, Australia), part of ANSTO. The development of the macro ATR-FTIR device used in this study was funded as part of the Science Projects at the Australian Synchrotron, and has been made available to users of the IRM Beamline. The authors wish to acknowledge Mr. Alan Easdon from the Australian Synchrotron, for his substantial contribution to the design and mechanical works associated with the development of this device. This work was performed in part at the Melbourne Centre for Nanofabrication (MCN) in the Victorian Node of the Australian National Fabrication Facility (ANFF). The Monash team at Centre for Biospectroscopy is supported by an Australian Research Council. MJH is supported by the Dementia Australia Research Foundation, Mamutil New Investigator Project Grant (11646). MJH gratefully acknowledges travel funding provided by ANSTO, funded by the Australian Government.

References

1. M. J. Baker, J. Trevisan, P. Bassan, R. Bhargava, H. J. Butler, K. M. Dorling, P. R. Fielden, S. W. Fogarty, N. J. Fullwood, K. A. Heys, C. Hughes, P. Lasch, P. L. Martin-Hirsch, B. Obinaju, G. D. Sockalingum, J. Sulé-Suso, R. J. Strong, M. J. Walsh, B. R. Wood, P. Gardner and F. L. Martin, *Nat. Protocols*, 2014, **9**, 1771-1791.
2. B. R. Wood and D. McNaughton, in *Spectrochemical Analysis Using Infrared Multichannel Detectors*, eds. R. Bhargava and I. Levin, Blackwell, UK, 2005, pp. 204-233.
3. P. Heraud and M. J. Tobin, *Stem Cell Res.*, 2009, **3**, 12-14.
4. D. Naumann, D. Helm and H. Labischinski, *Nature*, 1991, **351**, 81-82.
5. L. M. Miller and P. Dumas, *Biochim. Biophys. Acta-Biomembr.*, 2006, **1758**, 846-857.
6. H.-Y. N. Holman, H. A. Bechtel, Z. Hao and M. C. Martin, *Anal. Chem.*, 2010, **82**, 8757-8765.
7. G. L. Carr, J. A. Reffner and G. P. Williams, *Rev. Sci. Instrum.*, 1995, **66**, 1490-1492.
8. G. L. Carr, *Rev. Sci. Instrum.*, 2001, **72**, 1613-1619.
9. M. C. Martin, N. M. Tsvetkova, J. H. Crowe and W. R. McKinney, *Appl. Spectrosc.*, 2001, **55**, 111-113.
10. J. Vongsvivut, P. Heraud, A. Gupta, T. Thyagarajan, M. Puri, D. McNaughton and C. J. Barrow, *Protist*, 2015, **166**, 106-121.
11. K. Thumanu, W. Tanthanuch, D. Ye, A. Sangmalee, C. Lorthongpanich, R. Parnpai and P. Heraud, *J. Biomed. Opt.*, 2011, **16**, 057005.
12. D. R. Whelan, K. R. Bambery, L. Puskar, D. McNaughton and B. R. Wood, *Analyst*, 2013, **138**, 3891-3899.
13. N. J. Harrick, *Internal reflection spectroscopy*, John Wiley & Sons, NY, 1967.
14. S. G. Kazarian and K. L. A. Chan, *Analyst*, 2013, **138**, 1940-1951.
15. L. Lewis and A. J. Sommer, *Appl. Spectrosc.*, 1999, **53**, 375-380.
16. L. Lewis and A. J. Sommer, *Appl. Spectrosc.*, 2000, **54**, 324-330.
17. A. J. Sommer, L. G. Tisinger, C. Marcott and G. M. Story, *Appl. Spectrosc.*, 2001, **55**, 252-256.
18. B. M. Patterson and G. J. Havrilla, *Appl. Spectrosc.*, 2006, **60**, 1256-1266.
19. B. M. Patterson, G. J. Havrilla, C. Marcott and G. M. Story, *Appl. Spectrosc.*, 2007, **61**, 1147-1152.
20. S. G. Kazarian and K. L. A. Chan, *Biochim. Biophys. Acta-Biomembr.*, 2006, **1758**, 858-867.
21. K. L. A. Chan and S. G. Kazarian, *Appl. Spectrosc.*, 2008, **62**, 1095-1101.
22. K. L. A. Chan and S. G. Kazarian, *Appl. Spectrosc.*, 2003, **57**, 381-389.
23. S. G. Kazarian and K. L. A. Chan, *Appl. Spectrosc.*, 2010, **64**, 135A-152A.
24. K. L. A. Chan and S. G. Kazarian, *Chem. Soc. Rev.*, 2016, **45**, 1850-1864.
25. N. L. Benbow, J. L. Webber, P. Pawliszak, D. A. Sebben, T. T. M. Ho, J. Vongsvivut, M. J. Tobin, M. Krasowska and D. A. Beattie, *Sci. Rep.*, 2018, **8**, 17804.
26. D. Perez-Guaita, K. Kochan, M. Martin, D. W. Andrew, P. Heraud, J. S. Richards and B. R. Wood, *Vib. Spectrosc.*, 2017, **91**, 46-58.
27. K. L. Summers, N. Fimognari, A. Hollings, M. Kiernan, V. Lam, R. J. Tidy, D. Paterson, M. J. Tobin, R. Takechi, G. N. George, I. J. Pickering, J. C. Mamo, H. H. Harris and M. J. Hackett, *Biochemistry*, 2017, **56**, 4107-4116.
28. M. J. Hackett, J. A. McQuillan, F. El-Assaad, J. B. Aitken, A. Levina, D. D. Cohen, R. Siegele, E. A. Carter, G. E. Grau, N. H. Hunt and P. A. Lay, *Analyst*, 2011, **136**, 2941-2952.
29. M. J. Hackett, C. J. Britz, P. G. Paterson, H. Nichol, I. J. Pickering and G. N. George, *ACS Chem. Neurosci.*, 2015, **6**, 226-238.
30. M. J. Tobin, J. Vongsvivut, D. E. Martin, K. H. Sizeland, M. J. Hackett, R. Takechi, N. Fimorgnari, V. Lam, J. C. Mamo, E. A. Carter, B. Swarbrick, P. A. Lay, D. A. Christensen, D. Perez-Guaita, E. Lowery, P. Heraud, B. R.Wood, L. Puskar and K. R. Bambery, *Infrared Phys. Technol.*, 2018, DOI: 10.1016/j.infrared.2018.06.022.
31. V. K. Truong, M. Stefanovic, S. Maclaughlin, M. Tobin, J. Vongsvivut, M. Al Kobaisi, R. J. Crawford and E. P. Ivanova, *J. Vis. Exp.*, 2016, DOI: doi:10.3791/54309, e54309.
32. M. Ryu, A. Balcytis, X. Wang, J. Vongsvivut, Y. Hikima, J. Li, M. J. Tobin, S. Juodkazis and J. Morikawa, *Sci. Rep.*, 2017, **7**, 7419.
33. J. Vongsvivut, V. K. Truong, M. Al Kobaisi, S. Maclaughlin, M. J. Tobin, R. J. Crawford and E. P. Ivanova, *PLOS ONE*, 2017, **12**, e0188345.
34. R. J. Tidy, V. Lam, N. Fimognari, J. C. Mamo and M. J. Hackett, *Vib. Spectrosc*, 2017, **91**, 68-76.
35. A. Savitzky and M. J. E. Golay, *Anal. Chem.*, 1964, **36**, 1627–1639.
36. B. N. Dorakumbura, R. E. Boseley, T. Becker, D. E. Martin, A. Richter, M. J. Tobin, W. van Bronswjik, J. Vongsvivut, M. J. Hackett and S. W. Lewis, *Analyst*, 2018, DOI: 10.1039/C7AN01615H.

37. S. Nunna, C. Creighton, B. L. Fox, M. Naebe, M. Maghe, M. J. Tobin, K. Bambery, J. Vongsvivut and N. Hameed, *J. Mater. Chem. A*, 2017, **5**, 7372-7382.
38. J. A. Bailey, R. B. Dyer, D. K. Graff and J. R. Schoonover, *Appl. Spectrosc.*, 2000, **54**, 159-163.
39. G. L. Carr and G. P. Williams, *In "Accelerator-Based Infrared Sources and Applications", SPIE Conf. Proc.*, 1997, **v3153**, 51.
40. P. Bassan, H. J. Byrne, J. Lee, F. Bonnier, C. Clarke, P. Dumas, E. Gazi, M. D. Brown, N. W. Clarke and P. Gardner, *Analyst*, 2009, **134**, 1171-1175.
41. P. Bassan, H. J. Byrne, F. Bonnier, J. Lee, P. Dumas and P. Gardner, *Analyst*, 2009, **134**, 1586-1593.
42. A. F. Slater, W. J. Swiggard, B. R. Orton, W. D. Flitter, D. E. Goldberg, A. Cerami and G. B. Henderson, *Proc. Natl. Acad. Sci. USA*, 1991, **88**, 325-329.
43. D. Perez-Guaita, K. M. Marzec, A. Hudson, C. Evans, T. Chernenko, C. Matthäus, M. Miljkovic, M. Diem, P. Heraud, J. S. Richards, D. Andrew, D. A. Anderson, C. Doerig, J. Garcia-Bustos, D. McNaughton and B. R. Wood, *Chem. Rev.*, 2018, **118**, 5330-5358.
44. S. Roy, D. Perez-Guaita, D. W. Andrew, J. S. Richards, D. McNaughton, P. Heraud and B. R. Wood, *Anal. Chem.*, 2017, **89**, 5238-5245.
45. J. N. Alumasa, A. P. Gorka, L. B. Casabianca, E. Comstock, A. C. de Dios and P. D. Roepe, *J. Inorg. Biochem.*, 2011, **105**, 467-475.
46. D. Perez-Guaita, D. Andrew, P. Heraud, J. Beeson, D. Anderson, J. Richards and B. R. Wood, *Faraday Discuss.*, 2016, **187**, 341-352.
47. D. Perez-Guaita, K. Kochan, M. Batty, C. Doerig, J. Garcia-Bustos, S. Espinoza, D. McNaughton, P. Heraud and B. R. Wood, *Anal. Chem.*, 2018, **90**, 3140-3148.
48. M. J. Hackett, F. Borondics, D. Brown, C. Hirschmugl, S. E. Smith, P. G. Paterson, H. Nichol, I. J. Pickering and G. N. George, *ACS Chem. Neurosci.*, 2013, **4**, 1071-1080.
49. M. J. Hackett, S. Caine, X. Liu, T. E. May and F. Borondics, *Vib. Spectrosc*, 2015, **77**, 51-59.
50. M. Z. Kastyak-Ibrahim, M. J. Nasse, M. Rak, C. Hirschmugl, M. R. Del Bigio, B. C. Albensi and K. M. Gough, *NeuroImage*, 2012, **60**, 376-383.
51. L. Samuels, L. Kunst and R. Jetter, *Annu. Rev. Plant Biol.*, 2008, **59**, 683-707.
52. T. Shepherd and D. W. Griffiths, *New Phytol.*, 2006, **171**, 469-499.
53. M. Shimojima and H. Ohta, *Prog. Lipid Res.*, 2011, **50**, 258-266.
54. M. J. Steinbauer, N. W. Davies, C. Gaertner and S. Derridj, *Aust. J. Bot.*, 2009, **57**, 474-485.
55. G. E. J. Poinern, X. T. Le and D. Fawcett, *Nanotechnology, science and applications*, 2011, **4**, 113.

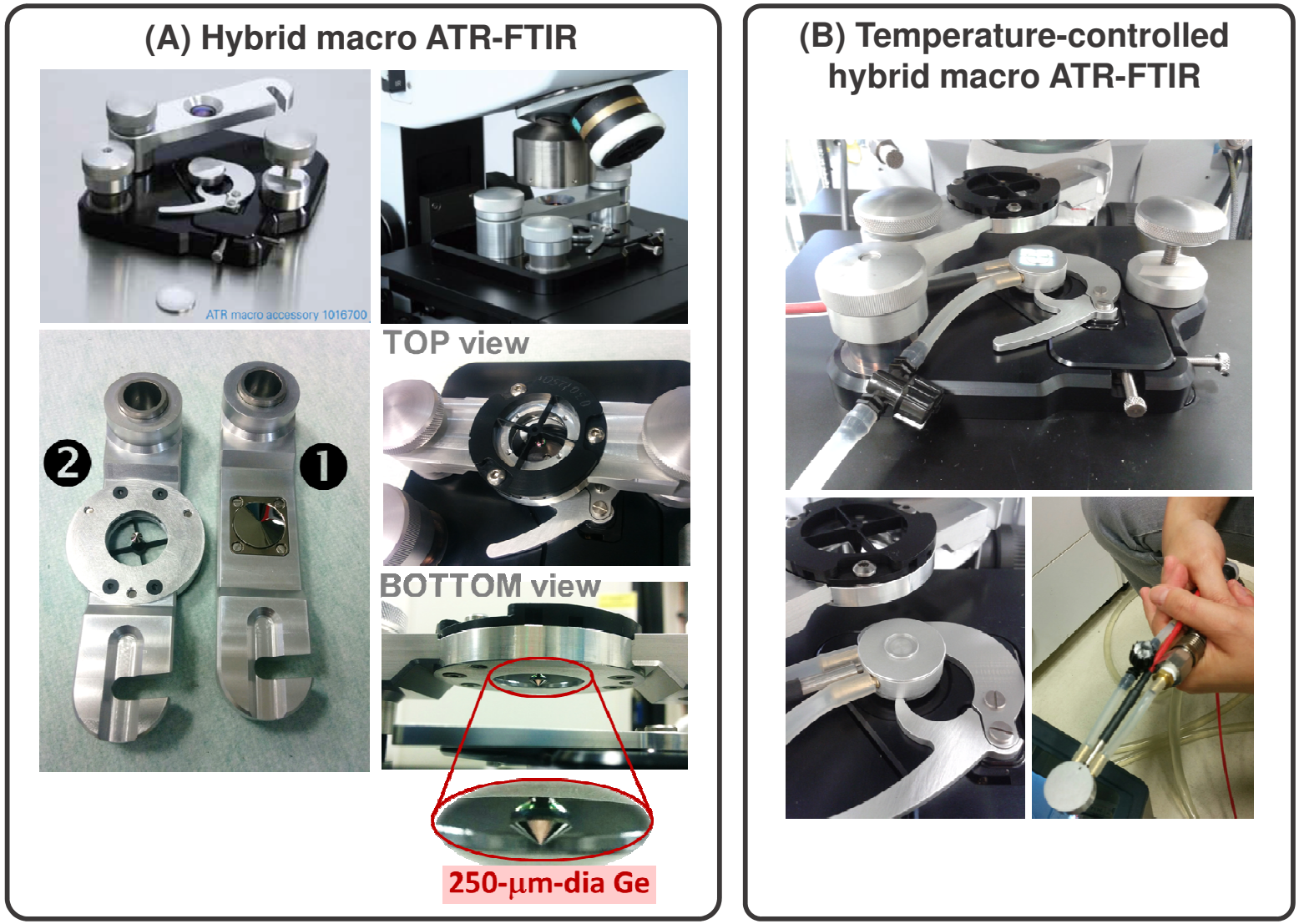

Figure 1. (A) Hybrid macro ATR-FTIR device, showing the standard macro ATR-FTIR unit (top) and the adaptation of cantilever arm to couple with the smaller diameter Ge micro-ATR crystal ❷, compared to the original 1 mm diameter Ge macro-ATR crystal ❶ (bottom). (B) Modification of the sample stage to couple with a temperature control unit, allowing water circulation for temperature-dependent studies.

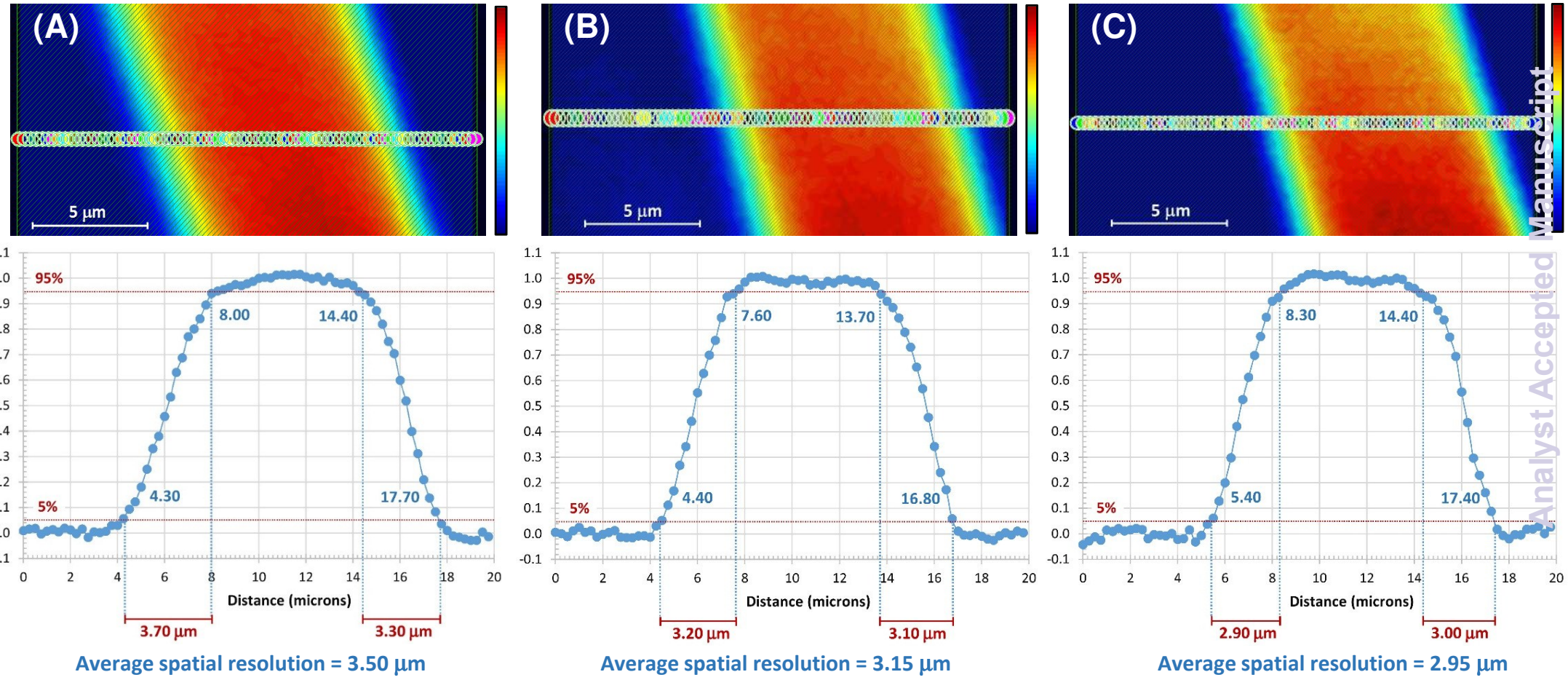

Figure 2. Spatial resolution evaluated by 5%–95% line scan approach according to the Rayleigh criterion. The synchrotron macro ATR-FTIR chemical maps of a photoresist polymer bar were acquired using 250 µm diameter Ge tip at 0.25 µm step interval and three smallest projected apertures of 3.13 µm (A), 2.50 µm (B) and 1.88 µm (C), respectively. The intensities in the chemical maps and their corresponding spatial resolution plots were calculated based on normalized intensities at 2925 cm^{-1} for ν_{as}(C–H) stretching mode, with red and blue representing areas with high and low intensities, respectively.

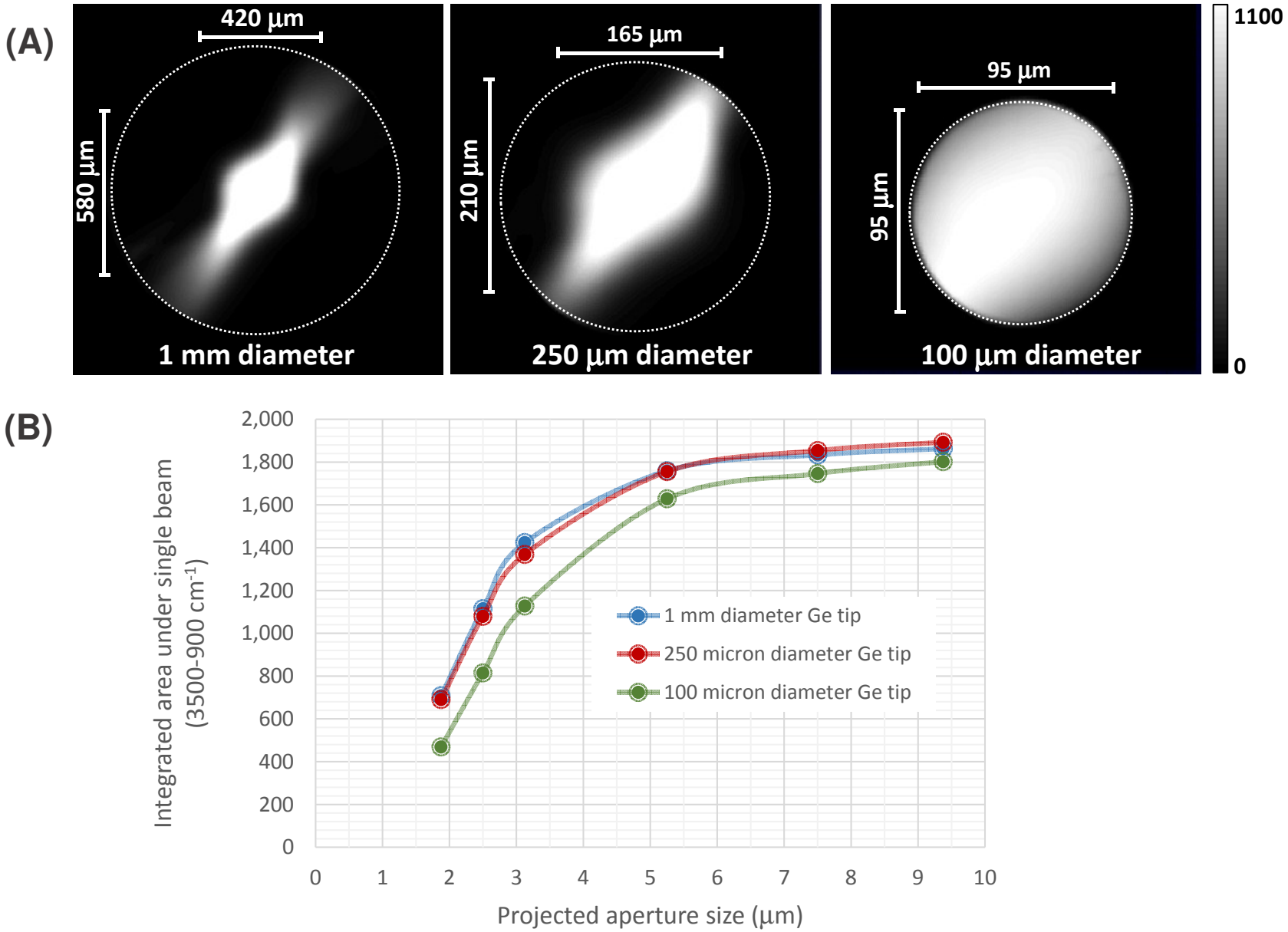

Figure 3. (A) Throughput of mapped beam relative to the size of the flat sensing surface of the Ge ATR crystals (in dashed circles), observed for the tip diameters of 1 mm, 250 µm and 100 µm, shown in linear grayscale from left to right, respectively. The measurement was performed using the projected aperture size of 3 µm and the throughput intensities were calculated based on integrated areas under single beam spectra in 900–3500 cm^{-1} region, with white and black representing areas with high and low throughputs, respectively. (B) Plots of throughputs as a function of projected aperture size, observed for the three tip sizes.

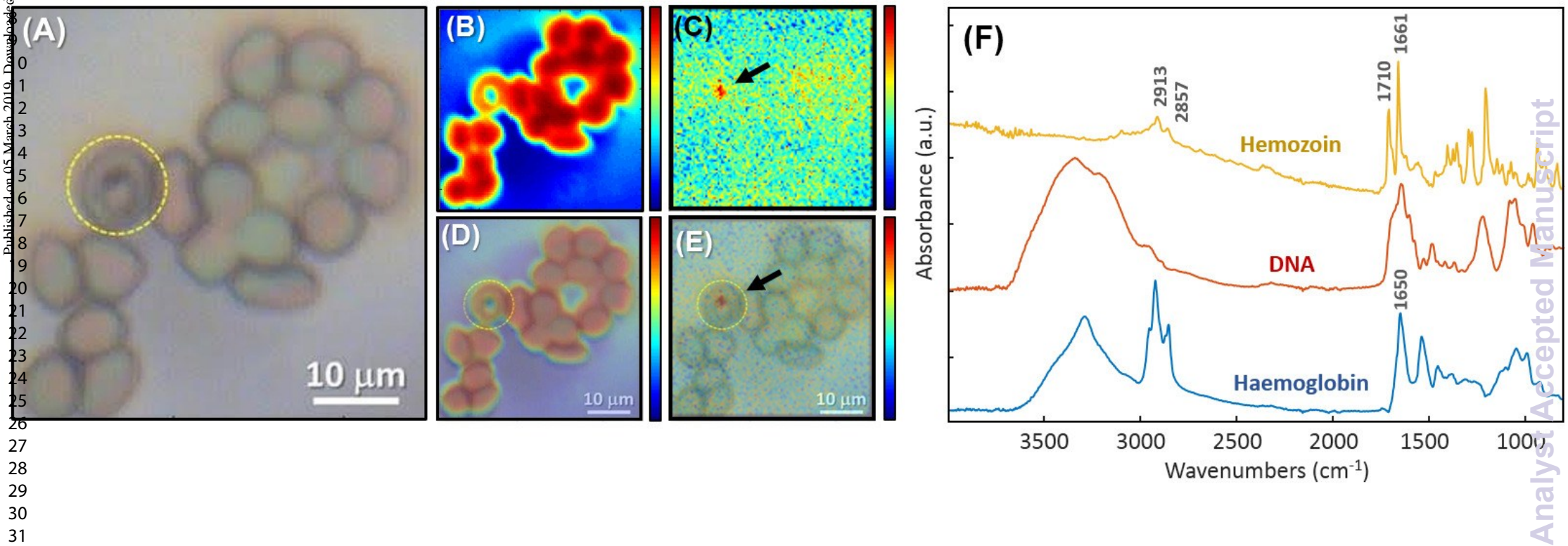

Figure 4. Synchrotron FTIR images of RBCs obtained using macro ATR-FTIR at 2 µm step resolution. (A) Visible image denoting the presence of a parasite in yellow circumference. (B) Intensity map of the Amide I band (1650 cm^{-1}). (C) Intensity map of the integrated area of the second derivative band minimum at the characteristic band of Hz (1710 cm^{-1}). (B-C) Red indicates high intensity and blue indicates low intensity. (D-E) Overlay of images B and C with the visible images, respectively. (F) Reference ATR-FTIR spectra of standards of hemozoin, DNA and haemoglobin from top to bottom, respectively.

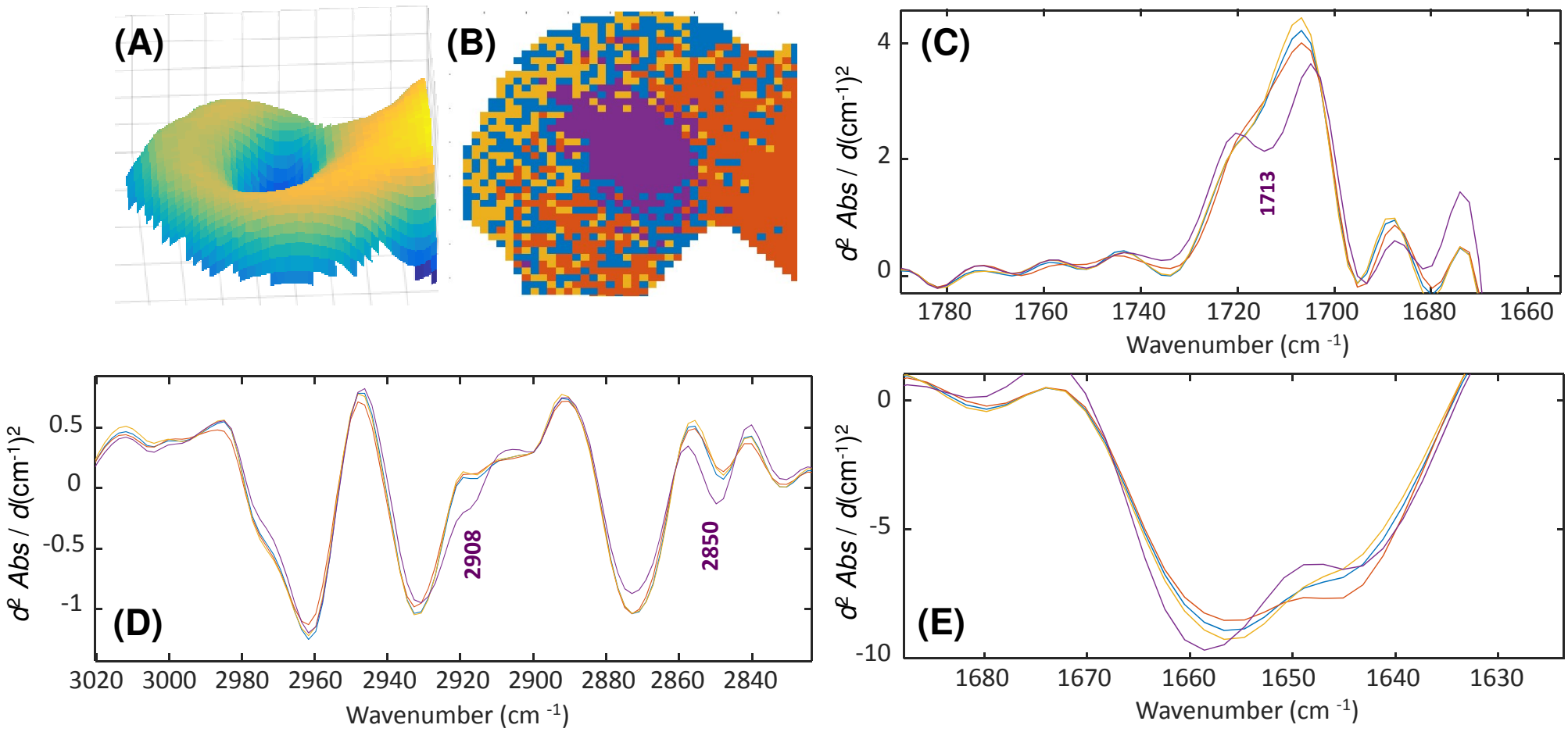

Figure 5. Synchrotron FTIR imaging of a malaria-infected RBC obtained using the macro ATR-FTIR technique at 0.50 µm step interval. (A) 3D intensity image of the Amide I band (1640 cm^{-1}) in the RBC infected with a parasite. (B) Cluster image performed over the hyperspectral image using second derivative, standard normal variate and mean centering, as pre-processing approach. (C-E) Average second derivative spectra from different classes obtained in the K-means cluster analysis. The colours of each average spectra are similar to those used in the cluster image (B), and thereby indicate their locations on the infected RBC.

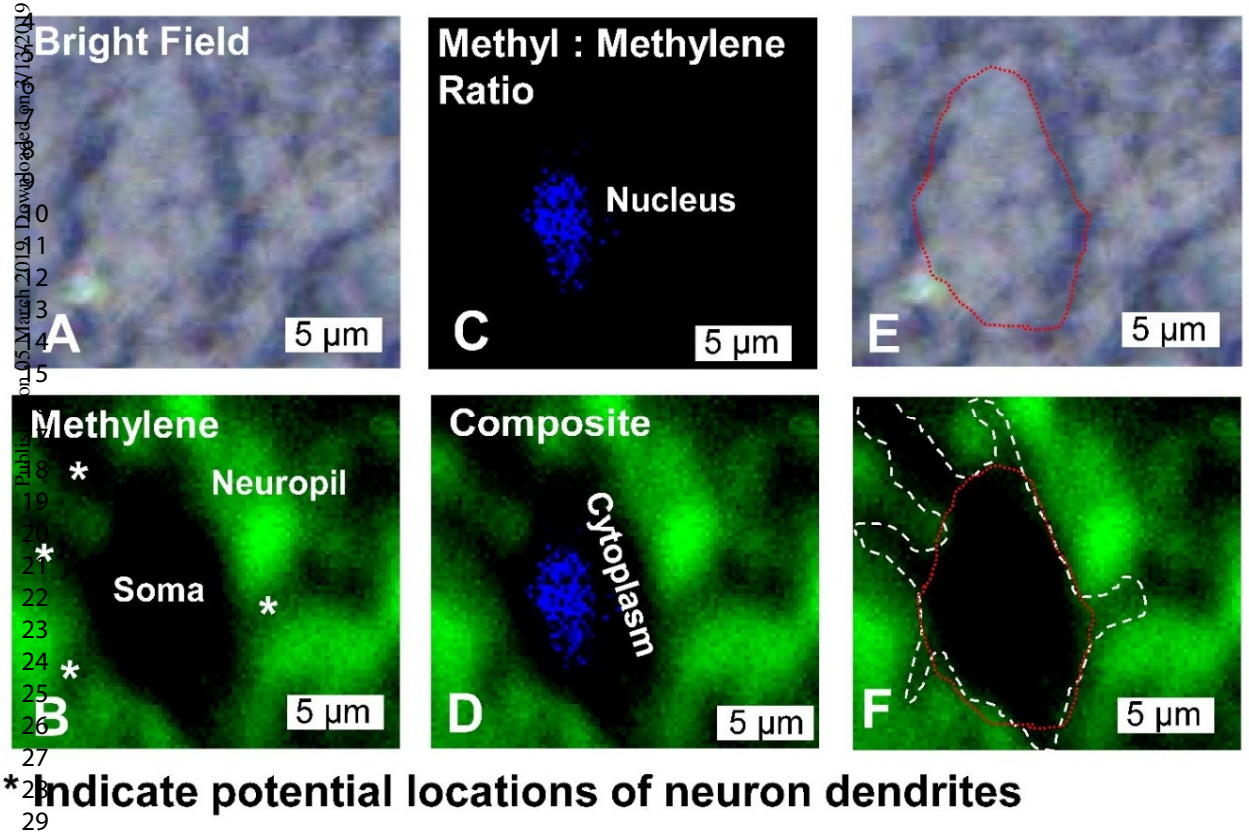

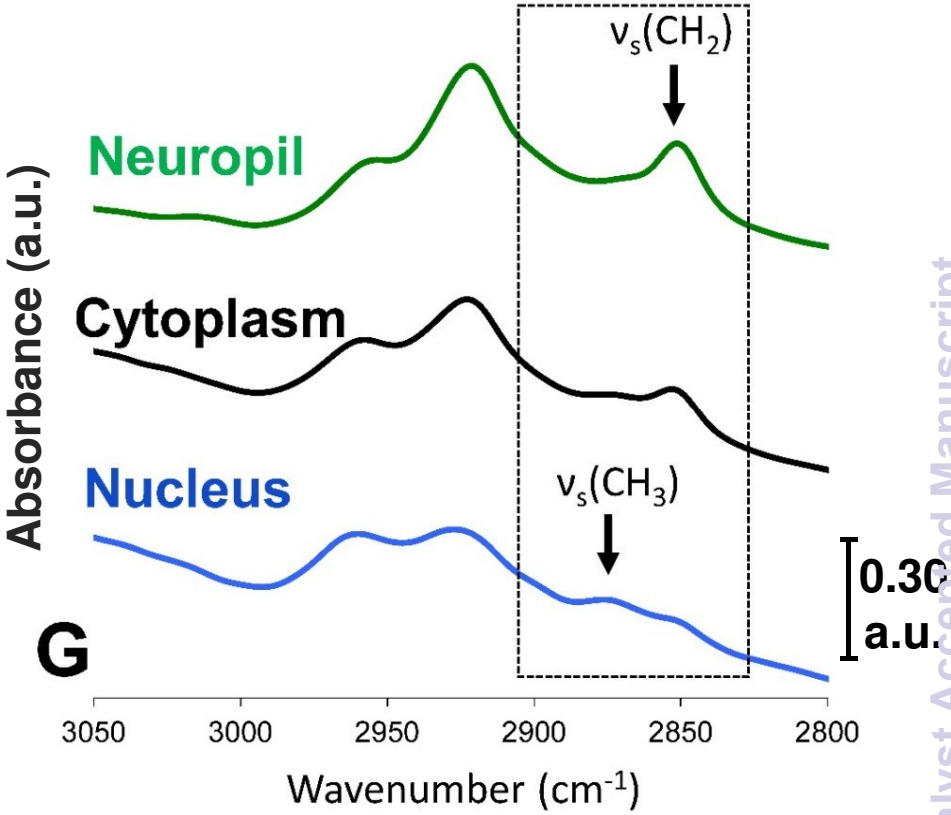

Figure 6. Synchrotron ATR-FTIR mapping of neurons within brain tissue provides the ability to resolve sub-cellular organelles such as the nucleus, and potentially dendritic branches. (A) Poor image contrast is observed in the unstained tissue; however, (B) false-colour images of methylene content, as a spectroscopic marker for lipid distribution (green) reveals the location of the neuron cell body (soma) that is low in lipid content (absence of green) compared to higher relative lipid content within the neuropil. In addition, regions of low lipid content radiate out from the neuron soma, through the neuropil, which is consistent with dendrite morphology. (C) The ratio of methyl to methylene content reveals the distribution of the neuron nucleus (blue), and (D) a two-colour overlay enables visualisation of the nucleus (blue) within the neuron soma (black) and surrounding neuropil (green). (E, F) The outlines of the neuron and dendrites have been sketched in red and white, respectively, on images presented in A and B. (G) Representative ATR-FTIR spectra from the nucleus (blue), neuron cytoplasm within the soma (black) and neuropil (green), with black arrows highlighting spectroscopic features that reflect that high lipid content of the neuropil, and high relative methyl content of the nucleus.

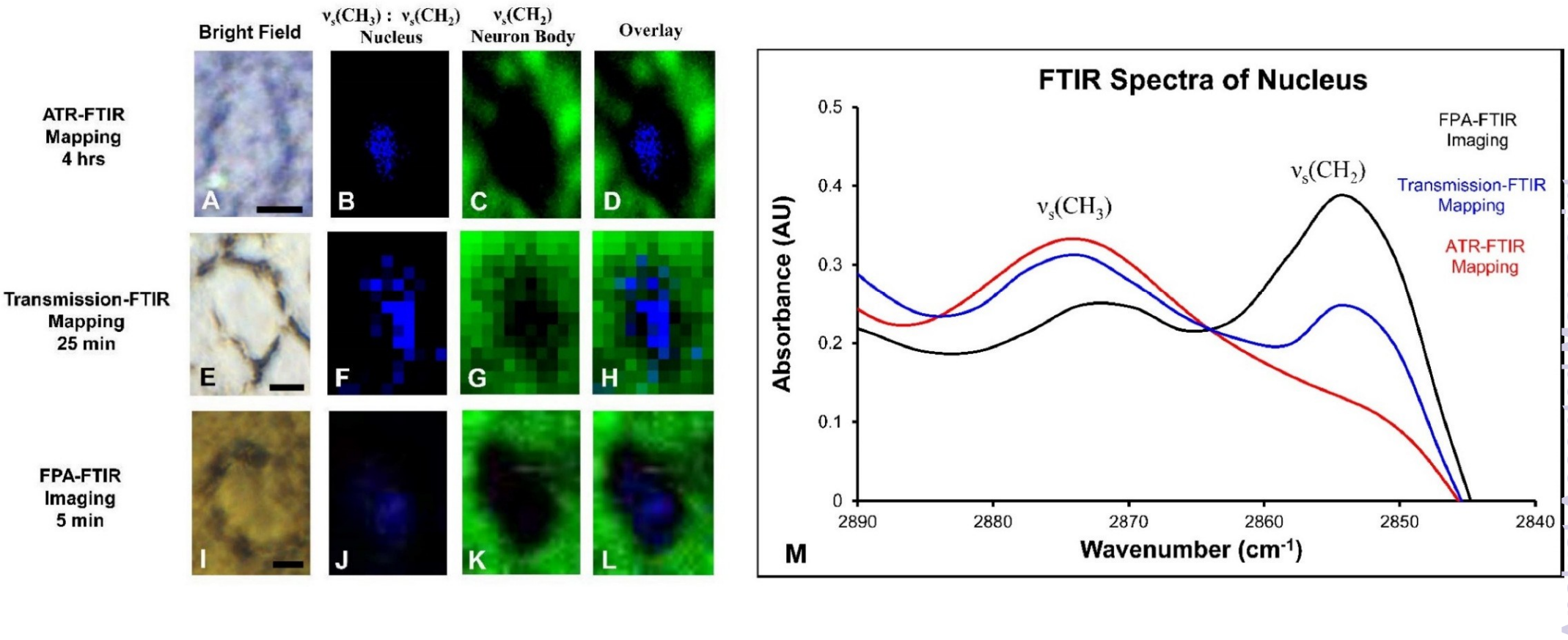

Figure 7. Comparison of synchrotron (A-D) ATR-FTIR mapping, (E-H) transmission-FTIR mapping, and (I-L) FPA-FTIR imaging of brain neurons. (A, E, I) Bright-field microscopy images of the unstained neuron prior to imaging, (B, F, J) localisation of nucleus based on ratio of $\nu_s(CH_3)$ to $\nu_s(CH_3)$ absorbance, (C, G, K) localisation of neuropil (green) and neuron body (black) based on $\nu_s(CH_2)$ absorbance, and (D, H, L) overlay image showing nuclei within neuron body. Image parameters (pixel size, projected aperture size, theoretical diffraction limit at 2852 cm^{-1}) are: ATR-FTIR mapping (0.25, 1.88, 3.56 µm), transmission-FTIR mapping (1.0, 4.2, 3.5 µm), FPA-FTIR imaging (0.77, no aperture, 3.3 µm). (M) Representative spectra extracted from the nucleus in each image, highlighting the increased signal from $\nu_s(CH_2)$ absorbance at 2852 cm^{-1} due to spectral blending with the cytoplasm in transmission-FTIR mapping and FPA-FTIR imaging measurements. The data collection times for each measurement are shown in the heading. Scale bar = 5 µm.

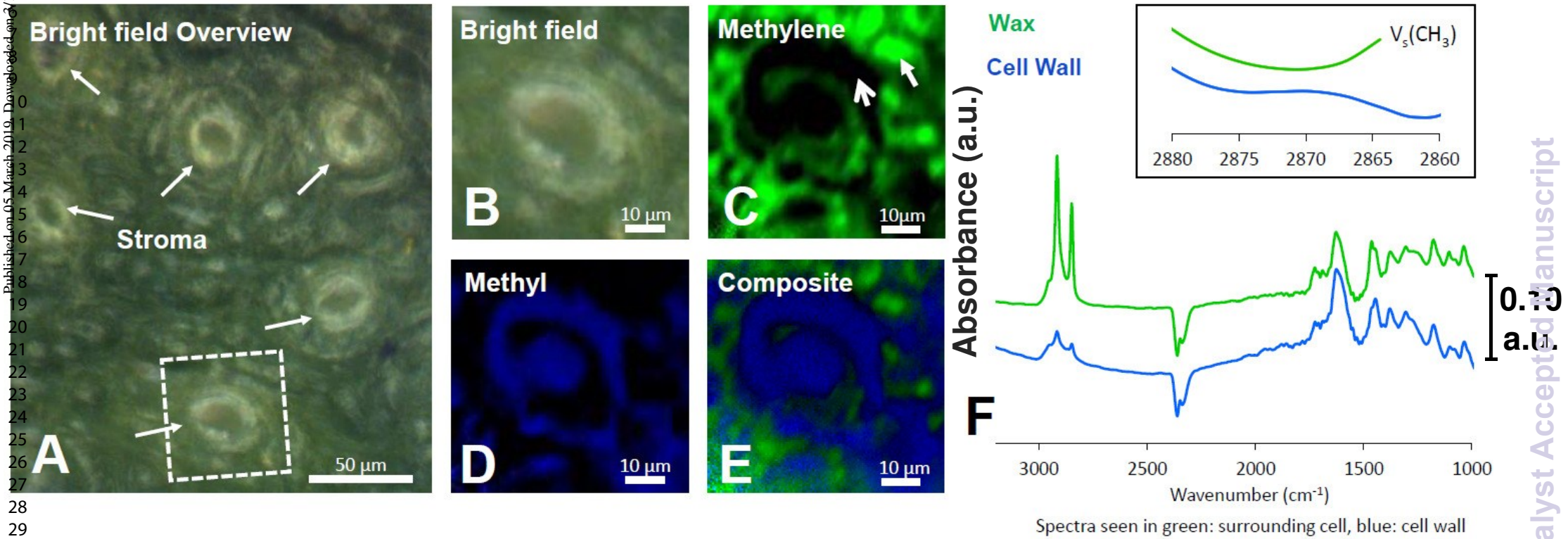

Figure 8. Synchrotron macro ATR-FTIR provides sub-micron mapping of epicuticular wax distribution on *Eucalyptus* leaves: (A) overview bright-field image of leaf surface, (B) imaged region on the leaf, (C) false-colour image of methylene groups (green) showing epicuticular wax distribution, (D) false-colour image of methyl groups (blue) showing the location of cell walls and stroma cell, (E) composite image showing high epicuticular wax content bordered cell walls, (F) representative synchrotron macro ATR-FTIR spectra showing key differences in methyl and methylene groups of cells wall and epicuticular waxes.

Sub-cellular mapping using synchrotron macro ATR-FTIR microspectroscopy at Australian Synchrotron IR Beamline